6-DOF Flight Dynamics of Laser-Boosted Vehicle Driven by Blast Wave

IEPC-2013-179

Presented at the 33rd International Electric Propulsion Conference,
The George Washington University, Washington, D.C., USA
October 6–10, 2013

Masayuki Takahashi* and Naofumi Ohnishi†
Tohoku University, Sendai, Miyagi, 980-8579, Japan

For examining flight performance of kg-order weight laser propulsion vehicle, scaling theory for the vehicle mass, the vehicle size, and the input energy is constructed to maintain a dynamical equivalence between the laboratory scale and the actual launch scale. The scaling law based on the equations of motion is confirmed by the numerical simulation for the impulse generation by the blast wave with a single pulse. Restriction of the kinetic scaling for the single pulse is assessed through the simple vertical motion of the vehicle, and the limit vehicle velocity is estimated as 104 m/s. For multiple pulses, the stable beaming-flight of the 1-kg and 10-kg vehicles is achieved with an active control technique based on the genetic algorithm. The dynamical equivalence for the multiple pulses is also examined using the flight simulator.

Nomenclature

C_D	= drag coefficient
E	= deposited laser energy, J
E_0	= reference laser energy, J
$\mathbf{E}, \mathbf{F}, \mathbf{G}$	= inviscid flux vectors in the X-, Y-, Z-directions
$\tilde{\mathbf{E}}, \tilde{\mathbf{F}}, \tilde{\mathbf{G}}$	= viscous flux vectors in the X-, Y-, Z-directions
F_b	= thrust by blast wave, N
F_d	= aerodynamic drag, N
$\mathbf{F}_a$	= aerodynamic force vector, N
g	= acceleration of gravity, m/s^2
h	= flight altitude, m
I_{xx}, I_{yy}, I_{zz}	= moments of inertia in the X-, Y-, Z-directions, kg·m^2
$k_1,\ k_2,\ k_3,\ k_b$	= proportional constants of thrust, moment, moment of inertia, and impulse
L_a, M_a, N_a	= aerodynamic moments in the X-, Y-, Z-directions, Nm
L_g, M_g, N_g	= gravity gradient torques in the X-, Y-, Z-directions, Nm
m	= vehicle mass, kg
m_0	= reference vehicle mass, kg
$\mathbf{M}_a$	= aerodynamic moment vector, Nm
M_b	= moment driven by blast wave, Nm
$P,\ Q,\ R$	= vehicle angular velocities in the X-, Y-, Z-directions, rad/s
$\mathbf{Q}$	= conservative variable vector

*Graduate Student, Department of Aerospace Engineering, mtakahashi@rhd.mech.tohoku.ac.jp
†Associate Professor, Department of Aerospace Engineering, ohnishi@rhd.mech.tohoku.ac.jp

r	= spatial scale, m
r_0	= spatial reference scale, m
$R_{Eth,i}$	= threshold of centering feedback, m
R_{pre}	= previous translational position of vehicle, m
R_0	= current translational position of vehicle, m
S	= area scale, m^2
S_0	= reference area scale, m^2
t	= time, s
t^*	= characteristic time of blast wave propagation, s
u	= translational vehicle velocity, m/s
u_{lim}	= limit vehicle velocity for scaling, m/s
$U,\ V,\ W$	= vehicle velocities in the X-, Y-, Z-directions, m/s
$\mathbf{U}_e$	= vehicle velocity vector in reference system, m/s
$\mathbf{U}_{ec}$	= current vehicle velocity in reference system, m/s
w	= beam radius, m
w_0	= initial beam radius, m
x, y, z	= fluid calculation coordinate, m
X_a, Y_a, Z_a	= aerodynamic forces in the X-, Y-, Z-directions, N
X_g, Y_g, Z_g	= gravity forces in the X-, Y-, Z-directions, N
Y_E, Z_E	= vehicle position for the Y-, Z-directions in reference system, m
α	= angular offset, degree
Δt_b	= time interval of blast wave interaction, s
Δt_{b0}	= reference time interval of blast wave interaction, s
$\mathbf{\Delta U}_{e0}$	= variation of vehicle velocity by single pulse at standard altitude, m/s
$\mathbf{\Delta \Omega}_{e0}$	= variation of angular velocity by single pulse at standard altitude, rad/s
λ	= beam wavelength, m
μ	= laser absorption rate by plasma
Π	= evaluation function
Φ_d	= aerodynamic drag term, N/s
Φ_{d0}	= reference term of aerodynamic drag, N/s
Φ_t	= thrust term, N/s
Φ_{t0}	= reference thrust term, N/s
Φ_a	= angular moment term, Nm/s
Φ_{a0}	= reference term of angular moment, Nm/s
ρ	= ambient density, kg/m^3
ρ_0	= ambient density at standard altitude, kg/m^3
ω	= angular vehicle velocity, rad/s
$\mathbf{\Omega}_e$	= angular velocity vector in reference system, rad/s
$\mathbf{\Omega}_{ec}$	= current angular velocity in reference system, rad/s
ξ	= parameter of moment of inertia

I. Introduction

Business of a cosmic journey is gradually realized by an opening of Space Ship One program in the USA, but further technical innovation for space transportation is needed to utilize the space for atmospheric observation, business, and academic study instead of the conventional LO_2/LH_2 rocket system. Laser propulsion is a novel launch system employing high-power beam transmitted from a ground base with loading no or a little fuel on a vehicle.[1,2] Launching cost-down must be achieved because of its high reusability and repeatability by repaying the initial cost of huge laser oscillator on the ground.[3] In an aero-driving mode, the vehicle obtains impulsive thrust through interactions with strong blast wave induced by the laser beam in the atmosphere acting as a driving gas. The high-power repetitive pulse laser is irradiated to the vehicle from the ground base and is focused by a parabolic mirror installed on the vehicle. The gas breakdown occurs, and the blast wave that pushes the vehicle into higher altitude is generated at a focal spot (ring). However, no thrust is obtained if the vehicle cannot capture the laser beam, and the flight cannot be maintained.

Performance to ride on the laser beam line, called beam-riding performance, is crucial for obtaining the continuous thrust and maintaining the stable flight without the deviation from the laser beam.[4–9] The beam-riding performance is totally assessed by the translational and angular feedback performances against misalignment of the laser incident. When the laser is irradiated with lateral error with respect to the body axis, the vehicle should cancel out the lateral offset (centering performance). On the other hand, when the laser is not irradiated parallel to the vehicle axis, the angular restoring moment must be generated to reduce the angular offset (tipping performance). If the insufficient restoring forces and moments are generated for the lateral and angular offsets, the beam-riding flight becomes unstable by losing the posture control with the rapid growth of the lateral and angular offsets.

The "lightcraft" proposed by Myrabo[2] is one of the best beam-riding vehicles among the present laser propulsion vehicles. The flight test of the lightcraft was demonstrated using the high-power repetitive pulses, and a type-200 spinning lightcraft weighting 50 g was launched and achieved the 71-m altitude in 2001. With a gyro stabilization by the high speed axial spin, the lightcraft has excellent beam-riding performance for obtaining the lateral feedback force by the ring-shroud installed on the main body. The laser beam is reflected by the rear mirror and focused inside the shroud, and the interaction between the blast wave and the shroud pushes the vehicle back toward the center of the laser beam if the laser incident has lateral misalignment against the vehicle axis.[8] In past studies of the lightcraft, experiments were conducted to examine the recentering and angular impulses for only lateral offset with a single pulse.[5,6] Also, flight simulations were conducted with multiple pulses based on the experimental impulse data for only lateral offset.[4,6–8] However, in the actual flight, the laser incident condition is complicated due to the angular offset and the lateral-angular combined offset; thus, the flight trajectory is difficult to be predicted in terms of the lateral offset alone. State-of-the-art flight simulation is required for more precise prediction by including the vehicle's reactions against the angular and the combined offsets.

In our previous studies, we have developed a three-dimensional hydrodynamics code coupled with an orbital calculation code and a ray-tracing code.[10–12] The beam-riding flight of the lightcraft was reproduced using a vehicle reaction data-map for the lateral, angular, and lateral-angular combination offsets, and the flight altitude well agreed with the experimental flight data of the past demonstration. In addition, we proposed a laser active control concept by the genetic algorithm (GA) for obtaining the better flight performance, and the vehicle weighting 32.5 g can fly into km-order altitude with keeping the beam-riding strategy. However, it is necessary to discuss the feasibility of such a flight control technique for the scaled-up vehicle as the actual launch size. A kinetic scaling theory should be constructed to make a correlation between the laboratory scale and the actual launch scale. In the system scale-up, if a dynamical equivalence is maintained between the small scale in the laboratory and the larger scale for the actual launch, the flight test in the laboratory scale is finally meaningful for realizing the laser propulsion flight.

Objective of this study is constructing the scaling theory for maintaining the dynamical equivalence between the laboratory scale and the actual launch scale. The vehicle mass, the vehicle size, the moment of inertia, and the input energy are determined to keep the kinetic similarity based on the equations of motion for the translational and angular motions. Moreover, the scaling theory for the blast wave interaction is confirmed by the numerical simulation using our fluid-orbit coupling flight simulator.

II. Numerical Methods

Computational models in this paper are based on our previous works.[10–12] The thrust decay model by both beam expansion and density decreasing in higher altitude is updated in this paper.

II.A. Flowfield calculation

Flowfield around a high-speed spinning lightcraft is numerically solved to estimate forces and moments acting on the vehicle. To predict an unsteady flowfield involving a laser-induced blast wave, a reflected shock wave, and an expansion wave, the three-dimensional Navier-Stokes equation is numerically solved;

$$\frac{\partial \mathbf{Q}}{\partial t} + \frac{\partial (\mathbf{E} - \tilde{\mathbf{E}})}{\partial x} + \frac{\partial (\mathbf{F} - \tilde{\mathbf{F}})}{\partial y} + \frac{\partial (\mathbf{G} - \tilde{\mathbf{G}})}{\partial z} = \mathbf{0}. \tag{1}$$

Discretization is performed in a cell-centered finite volume manner.[13] The AUSM-DV method[14] is employed for numerical flux with the second-order MUSCL method.[15] In the MUSCL method, we choose characteristic variables as interpolation quantities and use a minmod limiter to fulfill the TVD condition. The numerical flux is calculated with a local rotation matrix to introduce a general curvilinear coordinate.[16,17]

The viscous flux is estimated by the second-order central difference method, and the viscous coefficient is determined by Sutherland's formula.[13] The Spalart-Allmaras model[18] with a fully-developed turbulence assumption due to the axial spin of the lightcraft is employed to introduce the effect of the turbulent flow. The LU-SSOR method[19,20] is utilized for obtaining a steady solution used as an initial flow for the spinning lightcraft to save consumption of computational time. Viscous flux Jacobians are ignored in the LU-SSOR method, which causes an instability in viscous flows; thus, the inviscid eigenvalues are modified using eigenvalues corresponding to the viscous terms to maintain a stability of the scheme.[21] By the extension of the viscous term eigenvalues, we can conduct the stable computation with CFL number of up to 20 using the LU-SSOR. Time integration for unsteady blast wave propagation is performed by the first-order explicit Euler method. Comparison of the fourth-order Runge-Kutta method and the first-order Euler method reveals no obvious discrepancy between them. The translational velocity and the angular velocity of the vehicle are subtracted from the flowfield to introduce the effect of vehicle motion. By introducing a coupling between the compressible fluid and rigid body motion of the vehicle, dynamic pressure induced by rapid vehicle motion acts as the lateral and angular drags.

II.B. Orbital calculation

A vehicle's flight trajectory is determined by solving six-degree-of-freedom (6-DOF) equations of motion using aerodynamic forces and moments estimated from the unsteady flowfield solution. With a strong interaction between the blast wave and the vehicle surface, the orbital calculation is coupled with the flowfield calculation to introduce effects of the unsteady vehicle motion. Based on the orbital calculation we can estimate the vehicle's position and posture at the next pulse.

The conservation of linear and angular momenta for a rigid body results in 6-DOF equations of motion expressed in the body-fixed coordinate system. The 6-DOF equations of motion for tracing the vehicle trajectory is given by

$$m(\dot{U} + QW - RV) = X_g + X_a, \tag{2}$$
$$m(\dot{V} + RU - PW) = Y_g + Y_a, \tag{3}$$
$$m(\dot{W} + PV - QU) = Z_g + Z_a, \tag{4}$$
$$I_{xx}\dot{P} + (I_{zz} - I_{yy})QR = L_g + L_a, \tag{5}$$
$$I_{yy}\dot{Q} + (I_{xx} - I_{zz})RP = M_g + M_a, \tag{6}$$
$$I_{zz}\dot{R} + (I_{yy} - I_{xx})PQ = N_g + N_a. \tag{7}$$

When the blast wave strongly interacts with the vehicle surface, the aerodynamic forces $\mathbf{F}_a = [X_a, Y_a, Z_a]^T$ and the aerodynamic moments $\mathbf{M}_a = [L_a, M_a, N_a]^T$ should be estimated by integrating the surface pressure distribution and the viscous stress from the flowfield solution in the body-fixed coordinate system. We also introduce gravity forces and gravity gradient torques as external gravity forces and moments acting on the vehicle.[22]

II.C. Fluid-orbit coupling method

Because the vehicle is instantaneously driven by the strong blast wave, we must introduce an effect of vehicle motion on the flowfield. We combine the flowfield and the orbital calculation to introduce the vehicle motion effect in the body-fixed coordinate system. In the flowfield computation, the time variations of translational velocities of the vehicle and angular velocities, which are estimated by the orbital calculation, are fed back to the flowfield calculation at each step except for a high-speed spin. For modeling effects of a rotating fluid due to the axial spin of the lightcraft, a rotational boundary condition is employed on the vehicle surface.[23]

The laser beam is irradiated to the vehicle when the rotating fluid settles to a steady state, and the dynamics of unsteady blast wave is predicted. Initial spin rate is set to 10,000 rpm based on a past study.[8]

Flowfield-orbital coupling calculation is employed until the forces from the blast wave can be ignored. After that, only 6-DOF equations of motion are integrated with the external forces and moments derived from aerodynamic coefficients of a non-spinning lightcraft.[8]

II.D. Energy deposition model for flowfield calculation

In order to introduce off-axis and/or inclined laser incidence, it is necessary to predict the spot position where the reflected laser is focused and the amount of energy to be deposited at the focal spot. We perform ray-tracing to determine the initial energy deposition.[24]

For making the impulse data-map with the lateral, angular, and lateral-angular combination offsets, a laser beam of 420 J is irradiated to the vehicle weighting 32.5 g.[8,10] The laser beam is numerically divided into ~3,000 rays for the energy deposition by ray-tracing. The laser intensity is set to be spatially uniform within a circular cross-section of 7.2-cm radius, and the repetition frequency of the pulse laser is set to 26 Hz. We search for the maximum energy density point in a circular plane around the vehicle axis in three-dimensional computation and input the beam energy to the source of the blast wave, so that the ratio of internal energy to kinetic energy is 5 to 2.[25] Ray-tracing is conducted on a denser grid to improve the accuracy of the energy deposition, and the deposited distribution is interpolated to the grid for flowfield computation. The efficiency of laser energy absorption by plasma is assumed to be 60 % so as to adjust the generated impulse to the experiment data.[8,10]

II.E. Vehicle reaction data-map for multiple-pulse calculation

Data-map for increments of translational and angular velocities for the 32.5-g vehicle with the 420-J laser was made with the parameters of y-, z-, and angular offsets via the flowfield-orbit coupling calculation for a single laser pulse in our previous study.[10] To save the computational load in the simulation of the multiple-pulse flight, impulsive vehicle motions driven by the blast wave are interpolated from this data-map. For simulating the larger vehicle scale with the higher energy input using the data-map, the conventional data-map should be scaled up by the theoretical and numerical analyses. Impulsive increments of translational and angular velocities are interpolated using the data-map and are added into the current vehicle velocities $\mathbf{U}_{ec}$ and angular velocities $\mathbf{\Omega}_{ec}$ in the reference coordinate as shown below;

$$\mathbf{U}_e = \mathbf{U}_{ec} + \Delta\mathbf{U}_{e0}, \tag{8}$$

$$\mathbf{\Omega}_e = \mathbf{\Omega}_{ec} + \Delta\mathbf{\Omega}_{e0}. \tag{9}$$

However, the axial spin rate is maintained because the axial spin of the vehicle is not affected by the impulsive blast wave. The 6-DOF equations of motion are solved with the aerodynamic coefficients to estimate the lateral and angular offsets at the next laser pulse. The flight trajectory for multiple pulses is calculated by repeating the above process.

II.F. Thrust decay model by beam expansion and density decreasing

Obtained thrust decreases with beam divergence and density decrease at higher altitude. The beam radius is simply modeled by Gaussian beam profile[26] with the beam wavelength λ of 1 μm, and the initial beam radius w_0 of 7.2 cm for the 32.5-g vehicle[3,8] . To analytically model the translational and angular impulse dependencies on both the input energy decrease and the ambient density lowering, the spherically symmetric Sedov solution[25] is used. From the Gaussian beam profile and the Sedov solution, Eqs. (8) and (9) are rewritten to model the decline of the translational and angular velocities;

$$\mathbf{U}_e = \mathbf{U}_{ec} + \left(\frac{\rho(h)}{\rho_0}\right)^{1/2}\left(\frac{w_0}{w(h)}\right)\Delta\mathbf{U}_{e0}, \tag{10}$$

$$\mathbf{\Omega}_e = \mathbf{\Omega}_{ec} + \left(\frac{\rho(h)}{\rho_0}\right)^{1/2}\left(\frac{w_0}{w(h)}\right)\Delta\mathbf{\Omega}_{e0}. \tag{11}$$

II.G. Laser position control using optimization method

To obtain a state flight, we control the position of the incident laser beam. It is necessary to determine the optimized incident position by monitoring the flight trajectory of the vehicle for keeping the beam-riding flight. The incident laser position is actively controlled using the genetic algorithm (GA) because it has good performance to avoid local optimal solution as compared with other optimization schemes. A real-coded type GA[27] is used to obtain better solution in comparison with a binary-coded GA. BLX-α model[27] is employed for a crossover in the GA. Minimal Generation Gap (MGG) model[28] is used for generation alternation while mutation is not installed in this study because the variety is maintained when the MGG model is combined with the BLX-α.

In this paper, the GA procedure is as follows. At first, twenty laser position vectors are randomly created. Parents are selected from this group, and the BLX-α is operated twenty times to generate forty children. After that, using the MGG model, two individuals are selected from the group including the original parents and children, and parents are replaced by these individuals. This process is repeated until an evaluation function becomes sufficiently small or the GA loop becomes 100 times. For the GA optimization, the evaluation function Π is defined by

$$\Pi = \begin{cases} R_0 & \text{if } R_{past} < R_{Eth,i} \text{ and } R_0 \geq R_{Eth,i}, \\ \alpha & \text{otherwise}, \end{cases} \tag{12}$$

where $R_{Eth,i}$ $(i = 1,\ 2,\ \cdots,\ 69)$ is defined in 69 stages as shown below;

$$R_{Eth,i} = (1 + 0.125(i-1)) \times 0.1. \tag{13}$$

The angular offset α is usually regarded as the evaluation function except for the vehicle passing across the threshold radii $R_{Eth,i}$.

III. Results

III.A. Dynamical equivalence theory

In our previous studies[10–12] based on the past experiments of the lightcraft,[2,8] the beam-riding flight of the 32.5-g lightcraft was successfully achieved using the laser active control by the GA optimization. To examine a stable flight of a larger vehicle in the actual satellite launch, it is necessary to scale up the impulse data-map with keeping the dynamical equivalence between the small scale of 32.5 g and the larger scale of 1 kg or 10 kg. The kinetic scaling theory can make a correlation between the laboratory scale and the actual scale of the satellite launch. To select the input energy and the moment of inertia with keeping the kinetic similarity for the mass increase, the theoretical analysis is conduced based on the equations of motion for the translational and angular directions.

The vehicle mass of the type 200-5/6 lightcraft[2] is increased as 1 kg and 10 kg to make the kinetic scaling law. The vehicle size is enlarged as the vehicle mass increasing with keeping mass density and geometric similarity, and then the reference length and the reference area are scaled up by the following forms;

$$r = \left(\frac{m}{m_0}\right)^{1/3} r_0,\ S = \left(\frac{m}{m_0}\right)^{2/3} S_0. \tag{14}$$

The scaling law for the moment of inertia is given by

$$I_i = \left(\frac{m}{m_0}\right)^{\xi} I_{i0}, \tag{15}$$

where $i = xx,\ yy$, and zz. The reference moment of inertia $I_{xx0},\ I_{yy0}$, and I_{zz0} are set to 465 $\mathrm{g \cdot cm^2}$ for the X axis, 603 $\mathrm{g \cdot cm^2}$ for the Y axis, and 603 $\mathrm{g \cdot cm^2}$ for the Z axis from the previous works, respectively.[8,10]

During the blast wave interaction, the translational and angular equations of motion are given by

$$\frac{\mathrm{d}u}{\mathrm{d}t} = -g + \Phi_t,\ \frac{\mathrm{d}\omega}{\mathrm{d}t} = \Phi_a, \tag{16}$$

where the thrust term and the angular moment term supplied by the blast wave are defined as $\Phi_t \equiv F_b/m$ and $\Phi_a \equiv M_b/I_i$, respectively. We can ignore the effect of the aerodynamic drag because the aerodynamic drag is smaller than the impulsive thrust during the blast wave interaction. To keep the dynamical equivalence between the scaled-up system and the reference system, the laser energy at one pulse and the moment of inertia should be determined to satisfy

$$\frac{\Phi_t}{\Phi_{t0}} = 1,\ \frac{\Phi_a}{\Phi_{a0}} = 1. \tag{17}$$

Here, the thrust and the external moment given by the blast wave are assumed by the following forms;

$$F_b \propto E,\ M_b \propto rE. \tag{18}$$

Based on Eqs. (14), (15), and (18), the thrust, the external moment, and the moment of inertia are modeled using proportional constants $k_1,\ k_2$, and k_3 as follows;

$$F_b = k_1 E,\ M_b = k_2 E m^{1/3},\ I_i = k_3 m^{\xi}. \tag{19}$$

By substituting Eq. (19) into Eq. (17), the dynamical equivalence conditions are rewritten as

$$\frac{\Phi_t}{\Phi_{t0}} = \left(\frac{E}{E_0}\right)\left(\frac{m}{m_0}\right)^{-1} = 1, \tag{20}$$

$$\frac{\Phi_a}{\Phi_{a0}} = \left(\frac{E}{E_0}\right)\left(\frac{m}{m_0}\right)^{1/3-\xi} = 1. \tag{21}$$

Because the input energy of one pulse E and the parameter of the moment of inertia ξ are calculated from Eqs. (20) and (21), E and I_i are obtained by the following forms;

$$E = E_0\left(\frac{m}{m_0}\right),\ I_i = I_{i0}\left(\frac{m}{m_0}\right)^{4/3}. \tag{22}$$

For the 10-kg vehicle case, the input energy E and the moments of inertia $I_{xx},\ I_{yy}$, and I_{zz} are determined to keep the dynamical equivalence by using Eq. (22);

$$E = 1.3 \times 10^5\ \mathrm{J},\ I_{xx} = 9.66 \times 10^{-2}\ \mathrm{kg \cdot m^2},\ I_{yy} = I_{zz} = 1.25 \times 10^{-1}\ \mathrm{kg \cdot m^2}. \tag{23}$$

On the other hand, for the 1-kg vehicle case, E, $I_{xx},\ I_{yy}$, and I_{zz} are calculated as follows;

$$E = 1.3 \times 10^4\ \mathrm{J},\ I_{xx} = 4.48 \times 10^{-3}\ \mathrm{kg \cdot m^2},\ I_{yy} = I_{zz} = 5.81 \times 10^{-3}\ \mathrm{kg \cdot m^2}. \tag{24}$$

The theoretical scaling for the input energy and the moment of inertia during the blast wave interaction is validated by our fluid-orbit coupling code. The single pulse with lateral y-offset of $(m/m_0)^{1/3} \times (-5)$ mm is irradiated by the ray-tracing method to assess the translational and angular velocities of the 10-kg and 1-kg vehicles. The vehicle size, the moment of inertia, and the deposited energy are determined by Eqs. (14) and (22) to maintain the dynamical equivalence in the translational and angular motions. The vehicle shape is kept among all the models even if the vehicle size is enlarged. For the blast wave calculation, the time scale is normalized by a characteristic time of the self-similar solution for the blast wave;[25]

$$t^* = \left\{\left(\frac{m}{m_0}\right)^{1/3} r_0\right\}^{5/2}\left(\frac{\rho}{\mu E}\right)^{1/2}. \tag{25}$$

In the simulations of the blast wave propagation, the dynamical equivalence is successfully maintained between the 10-kg case and 32.5-g case for the translational and angular motions (Fig. 1). For the 1-kg case, the translational and angular velocities also agree with the 32.5-g case. The conventional data-map can be employed for simulating the flight trajectory of the 10-kg and 1-kg vehicles with the multiple pulses because the dynamical equivalence is maintained for each case.

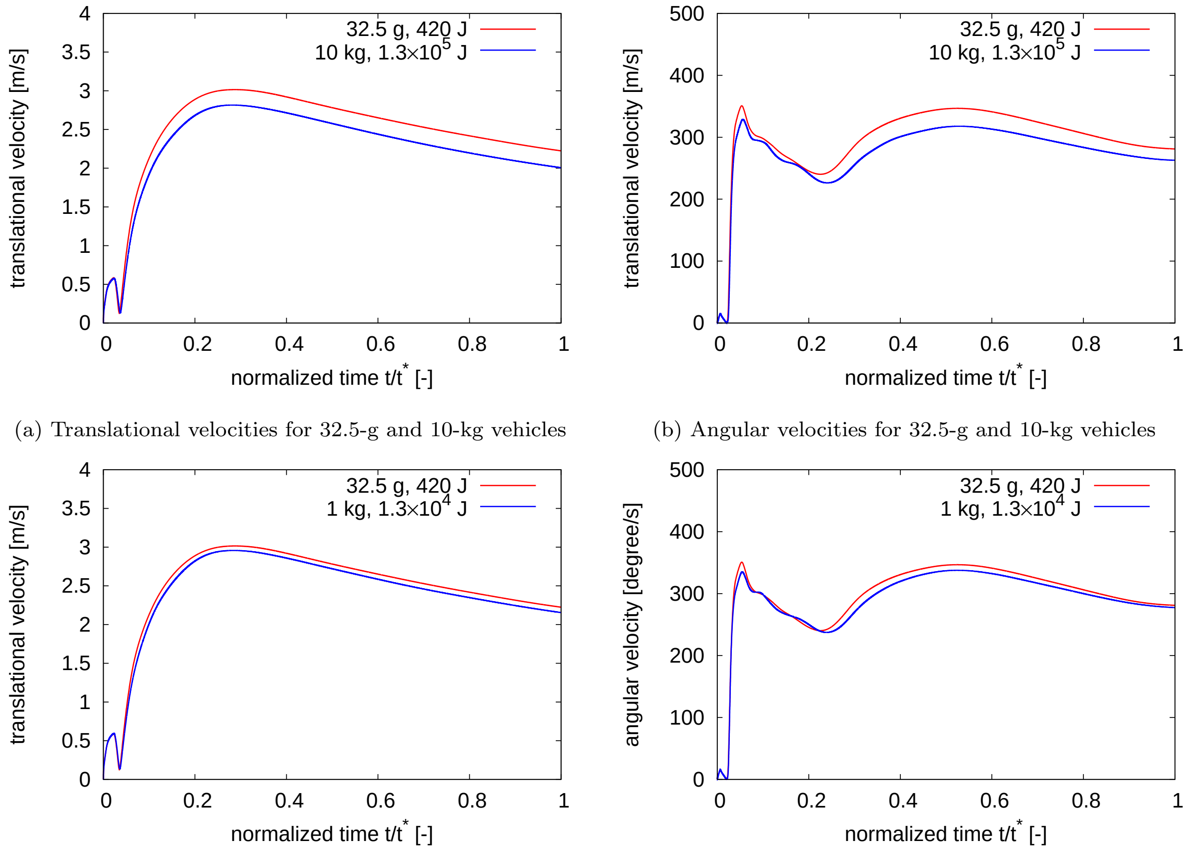

(a) Translational velocities for 32.5-g and 10-kg vehicles

(b) Angular velocities for 32.5-g and 10-kg vehicles

(c) Translational velocities for 32.5-g and 1-kg vehicles

(d) Angular velocities for 32.5-g and 1-kg vehicles

Figure 1. Time evolutions of translational and angular velocities for 32.5-g, 1-kg, and 10-kg vehicles.

III.B. Limitation of scaling theory

The theoretical scaling for the single pulse was confirmed by the numerical simulation, but there is a restriction of the scaling theory because the aerodynamic drag cannot be ignored with the vehicle velocity increase. So, it is necessary to assess the limit velocity for the flight scaling during the blast wave interaction.

By introducing the aerodynamic drag, the integration form of the 1-DOF equation of motion for the vertical velocity during the blast wave interaction is given by

$$\int du = \int -g\mathrm{d}t + \int \frac{F_b}{m}\mathrm{d}t - \int \frac{F_d}{m}\mathrm{d}t. \tag{26}$$

In Eq. (26), the aerodynamic drag effect cannot be ignored when the drag term becomes comparable with the thrust term in a high-speed flight, that is,

$$\int \frac{F_b}{m}\mathrm{d}t = \int \frac{F_d}{m}\mathrm{d}t. \tag{27}$$

The aerodynamic drag term is approximated using a time interval of the blast wave interaction Δt_b;

$$\int \frac{F_d}{m}\mathrm{d}t \approx \Delta t_b \frac{1}{2}\rho S C_D u^2. \tag{28}$$

The vehicle velocity u is replaced by u_{lim} when Eq. (27) holds, and u_{lim} is calculated by Eqs. (27) and (28) as shown below;

$$u_{lim} \approx \sqrt{\frac{\int F_b \mathrm{d}t}{\Delta t_b \frac{1}{2}\rho S C_D}}. \tag{29}$$

The limit velocity u_{lim} can be estimated when the time integration of the thrust driven by the blast wave $\int F_b \mathrm{d}t$ and the interaction time Δt_b are obtained by the numerical simulation. We assume that the time integration of the thrust is simply proportional to the input energy E;

$$\int F_b \mathrm{d}t \approx k_b E. \tag{30}$$

Using the characteristic time of the blast wave (Eq. (25)), the ratio of the time interval between the scaled-up system Δt_b and the reference system Δt_{b0} is given by

$$\frac{\Delta t_b}{\Delta t_{b0}} = \left(\frac{r}{r_0}\right)^{5/2} \left(\frac{E_0}{E}\right)^{1/2}. \tag{31}$$

From Eqs. (14), (22), and (31), the time interval Δt_b can be expressed by the ratio of the input energy E/E_0;

$$\Delta t_b = \Delta t_{b0} \left(\frac{E}{E_0}\right)^{1/3}. \tag{32}$$

From Eqs. (14) and (22), the reference area S is also estimated by the following form,

$$S = S_0 \left(\frac{E}{E_0}\right)^{2/3}. \tag{33}$$

By substituting Eqs. (30), (32), and (33) into Eq. (29), the limit velocity u_{lim} is calculated independent of the system size;

$$u_{lim} \approx \sqrt{\frac{k_b E}{\Delta t_{b0} (\frac{E}{E_0})^{1/3} \frac{1}{2} \rho S_0 (\frac{E}{E_0})^{2/3} C_D}} = \sqrt{\frac{k_b E_0}{\Delta t_{b0} \frac{1}{2} \rho S_0 C_D}}. \tag{34}$$

The time interval of the blast wave Δt_{b0} and the proportional constant k_b are to be numerically given using the coupling code. From the numerical simulation for the 32.5-g vehicle as the reference system, the proportional constant for the impulse k_b is estimated as 0.00011 (Fig. 2(a)). The time interval of the blast wave interaction Δt_{b0} is also estimated as about 1000 μs (Fig. 2(b)). With $E_0 = 420$ J, $\rho \approx 1.0$ kg/m^3, $C_D = 0.731$, $S_0 = 0.061^2\pi$ m^2, $k_b = 0.00011$, and $\Delta t_{b0} = 1000$ μs, the limit velocity u_{lim} is estimated to 104 m/s. Therefore, the kinetic scaling based on the equations of motion suggests that the aerodynamic effect cannot be ignored if the vehicle velocity becomes larger than $u_{lim} = 104$ m/s.

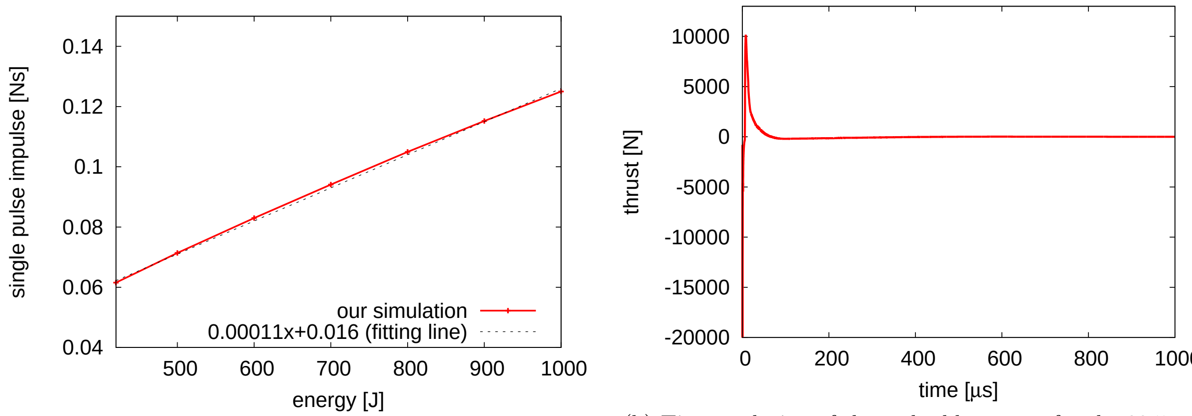

(a) Impulse dependence on input energy

(b) Time evolution of thrust by blast wave for the 32.5-g vehicle

Figure 2. Impulse dependence on input energy and time evolution of thrust.

III.C. Dynamical equivalence for multiple pulses

The scaling theory was constructed with keeping the dynamical equivalence for the single pulse, but there is no guarantee that the equivalence is maintained for the multiple-pulse flight. It is therefore necessary to confirm that the dynamical equivalence is maintained or not for the multiple-pulse flight.

Using the active laser control by the GA optimization,[11] the 6-DOF multiple-pulse simulations are conducted for the 32.5-g, 1-kg, and 10-kg vehicles with the initial offset of 5 mm. For three cases, the km-order flights are successfully achieved with keeping the beam-riding strategy by suppressing the angular offset (Fig. 3(a)). The identical velocities should be obtained for three cases if the dynamical equivalence is certainly maintained, but the vehicle velocities are different for each case (Fig. 3(b)). The dynamical equivalence is not maintained during the free flight of the pulse to pulse interval because the effective aerodynamic drag becomes smaller with increasing the vehicle mass.

During the pulse to pulse interval, the 1-DOF equation of motion for a vertical free flight is given by

$$\frac{\mathrm{d}u}{\mathrm{d}t} = -g - \frac{F_d}{m}. \tag{35}$$

With $F_d = \frac{1}{2}\rho S C_D u^2$, the drag term Φ_d is calculated by

$$\Phi_d = \frac{\frac{1}{2}\rho S C_D u^2}{m}. \tag{36}$$

Using Eqs. (14) and (36), the ratio of the drag term Φ_d/Φ_{d0} (index 0 denotes the reference system) results in

$$\frac{\Phi_d}{\Phi_{d0}} = \left(\frac{m_0}{m}\right)^{1/3} < 1. \tag{37}$$

The dynamical equivalence for the multiple pulses is not maintained because $\Phi_d/\Phi_{d0} \neq 1$ during the free flight. Because Φ_d/Φ_{d0} becomes smaller with increasing the vehicle mass, the vehicle velocity becomes larger. The scaling law of the reference area S should be determined for keeping the relation of $\Phi_d/\Phi_{d0} = 1$ to obtain the dynamical equivalence during the free flight.

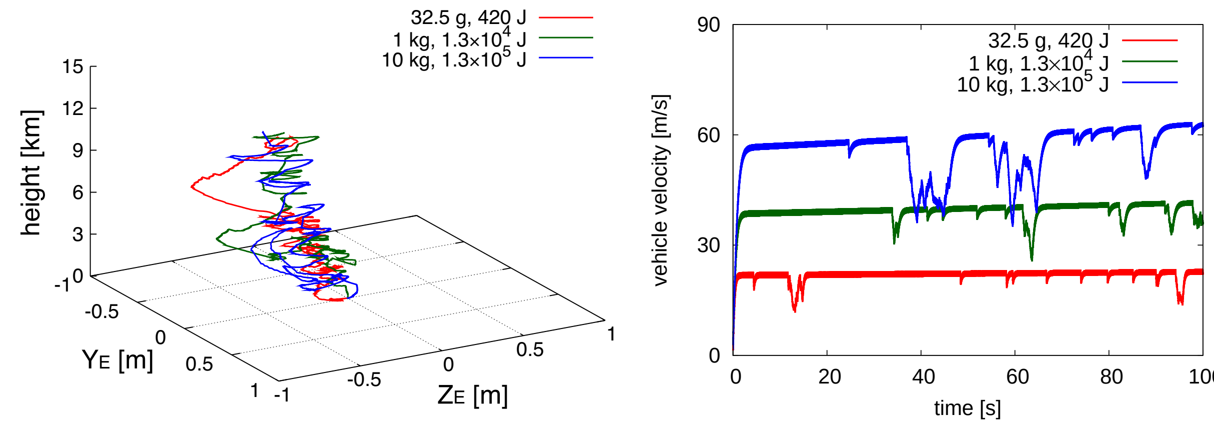

(a) 6-DOF flight trajectories

(b) Time evolution of vehicle velocities

Figure 3. Flight trajectories and vehicle velocities using scaled-up data.

IV. Conclusion

For predicting flight performance of the actual-weight vehicle, we construct the scaling theory for the vehicle size, the input energy, and the moment of inertia to maintain the dynamical equivalence between the laboratory scale and the actual launch scale of the laser propulsion flight. During the blast wave interaction, the translational and angular equations of motion are used to construct the kinetic scaling law. The theoretical analysis is confirmed by the numerical simulation of the blast wave interaction for the single pulse using the fluid-orbital coupling simulator. Because the effect of the aerodynamic drag becomes larger during the blast wave interaction, there is the limit velocity for the flight scaling. The limit velocity for the analytical scaling is estimated as 104 m/s based on the 1-DOF equation of motion for a vertical flight. Finally, the stable flight of the 1-kg and 10-kg vehicles with the multiple pulses is successfully achieved using the active laser control by the genetic algorithm. The dynamical equivalence for the multiple pulses is not maintained because the effective aerodynamic drag becomes smaller due to the larger inertia for the heavier vehicle. For the multiple-pulse flight, the scaling law of the vehicle reference area should be constructed for keeping the dynamical equivalence during the free flight of the pulse to pulse interval.

Acknowledgment

The computations in this work were performed on Nippon Electric Company (NEC) SX-9 model A and Silicon Graphics International (SGI) Altix UV1000 at Advanced Fluid Information Research Center, Institute of Fluid Science, Tohoku University. This work was supported by JSPS KAKENHI Grant Number H3255089.

References

[1]Mead, F. B., Jr., Messitt, D. G., and Myrabo, L. N., "Flight and Ground Tests of a Laser-Boosted Vehicle," AIAA Paper 98–3735, 1998.

[2]Myrabo, L. N., "World Record Flights of Beam-Riding Rocket Lightcraft: Demonstration of 'Disruptive' Propulsion Technology," AIAA Paper 2001–3798, 2001.

[3]Katsurayama, H., Komurasaki, K., and Arakawa, Y., "A Preliminary Study of Pulse-Laser Powered Orbital Launcher," *Acta Astronautica*, Vol. 65, 2009, pp. 1032–1041.

[4]Libeau, M., Myrabo, L. N., Filippelli, M., and Mclnerney, J., "Combined Theoretical and Experimental Flight Dynamics Investigation of a Laser-Propelled Vehicle," AIAA Paper 2002–3781, 2002.

[5]Libeau, M. and Myrabo, L. N., "Off-Axis and Angular Impulse Measurements on a Lightcraft Engine," *Beamed Energy Propulsion: Third International Symposium on Beamed Energy Propulsion, AIP Conference Proceedings*, Vol. 766, 2005, pp. 166–177.

[6]Kenoyer, D. A., Anderson, K. S., and Myrabo, L. N., "Calibration and Validation of a 6-DOF Laser Propelled Lightcraft Flight Dynamics Model vs. Experimental Data," *Beamed Energy Propulsion: Fifth International Symposium on Beamed Energy Propulsion, AIP Conference Proceedings*, Vol. 997, 2008, pp. 325–337.

[7]Kenoyer, D. A., Anderson, K. S., and Myrabo, L. N., "Trajectory Simulations for Laser-Launched Microsatellites Using A 7-DOF Flight Dynamics Model," *Proceedings of the ASME 2009 International Design Engineering Technical Conference & Computers and Information in Engineering Conference*, Vol. 4, 2009, pp. 21–29.

[8]Ballard, C. G., Anderson, K. S., and Myrabo, L. N., "Flight Dynamics and Simulation of Laser Propelled Lightcraft," *Journal of Computational and Nonlinear Dynamics*, Vol. 4, 2009, pp. 041005-1–041005-8.

[9]Scharring, S., Eckel, H. A., and Röser, H. P., "Beam-Riding Analysis of a Parabolic Laser-thermal Thruster," *Beamed Energy Propulsion: Seventh International Symposium on Beamed Energy Propulsion, AIP Conference Proceedings*, Vol. 1402, 2011, pp. 115–131.

[10]Takahashi, M. and Ohnishi, N., "Beam Riding Performance of Asymmetrically Propelled Laser Vehicle," *AIAA Journal*, Vol. 50, No. 11, 2012, pp. 2600–2608.

[11]Takahashi, M. and Ohnishi, N., "Performance Analysis of Beam Riding Vehicle with Motion Synchronized Laser Pulse," AIAA Paper 2012-3302, 2012.

[12]Takahashi, M. and Ohnishi, N., "Supersonic and Stable Flight of Beam Riding Vehicle Using Optimized Multiple Pulses," AIAA Paper 2013-0206, 2013.

[13]Hirsch, C., *Numerical Computation of Internal and External Flows*, Vol. 1, John Wiley and Sons, New York, 1984.

[14]Wada, Y. and Liou, M. S., "A Flux Splitting Scheme with High-Resolution and Robustness for Discontinuities," AIAA Paper 2006-1358, 2006.

[15]van Leer, B., "Toward the Ultimate Conservative Difference Scheme V, A Second-Order Sequel to Godunov's Method," *Journal of Computational Physics*, Vol. 32, Issue 1, 1979, pp. 101–136.

[16]Toro, E. F., *Riemann Solvers and Numerical Methods for Fluid Dynamics*, 3rd ed., Springer Press, New York, 2010.

[17]Toro, E. F. and Clarke, J. F., *Numerical Methods for Wave Propagation*, Kluwer Academic Publishers, London, 1998.

[18]Spalart, P. R. and Allmaras, S. R., "A One-Equation Turbulence Model for Aerodynamic Flows," AIAA Paper 92-0439, 1992.

[19]Jameson, A. and Yoon, S., "Lower-Upper Implicit Schemes with Multiple Grids for the Euler Equations," *AIAA Journal*, Vol. 25, 1987, pp. 929–935.

[20]Yoon, S. and Jameson, A., "Lower-Upper Symmetric-Gauss-Seidel Method for the Euler and Navier-Stokes Equations," *AIAA Journal*, Vol. 26, 1988, pp. 1025–1026.

[21]Obayashi, S. and Kuwahara, K., "An Approximate LU Factorization Method for the Compressible Navier-Stokes Equations," *Journal of Computational Physics*, Vol. 63, 1986, pp. 157–167.

[22]Skullestad, A."Modeling and Control of a Gravity Gradient Stabilised Satellite," *Modeling, Identification and Control*, Vol. 20, No. 1, 1999, pp. 3–25.

[23]Hirsch, C., *Numerical Computation of Internal and External Flows*, Vol. 2, John Wiley and Sons, New York, 1984.

[24]Born, M. and Wolf, E., *Principles of Optics*, 1st ed., Vol. 1, Pergamon Press, New York, 1959.

[25]Sedov, L. I., *Similarity and Dimensional Methods in Mechanics*, 10th ed., CRC Press, Florida, 1993.

[26]Saleh, B. E. A. and Teich, M. C., *Fundamentals of Photonics*, John Wiley and Sons, New York, 1991.

[27]Eshelman, L. J. and Schaffer, J. D., "Real-Coded Genetic Algorithms and Interval-Schemata," *Foundations of Genetic Algorithms 2: Proceedings of the Second Workshop on Foundations of Genetic Algorithms*, 1992, pp. 187–202.

[28]Sato, H., Yamamura, M., and Kobayashi, S., "Minimal Generation Gap Model for GAs Considering Both Exploration and Exploitation," *Conference Proceedings of the 4th International Conference on Fuzzy Logic, Neural Nets and Soft Computing*, 1996, pp. 494–497.